

Optical spin control and coherence properties of acceptor bound holes in strained GaAsXiayu Linpeng,¹ Todd Karin,² Mikhail V. Durnev,³ Mikhail M. Glazov^{3,4}, Rüdiger Schott,⁵ Andreas D. Wieck⁵, Arne Ludwig⁵ and Kai-Mei C. Fu^{1,6}¹*Department of Physics, University of Washington, Seattle, Washington 98195, USA*²*Lawrence Berkeley National Laboratory, Berkeley, California 94720, USA*³*Ioffe Institute, 194021 St.-Petersburg, Russia*⁴*Spin Optics Laboratory, Saint Petersburg State University, 198504 St. Petersburg, Russia*⁵*Lehrstuhl für Angewandte Festkörperphysik, Ruhr-Universität Bochum, D-44870 Bochum, Germany*⁶*Department of Electrical Engineering, University of Washington, Seattle, Washington 98195, USA* (Received 15 December 2020; revised 20 February 2021; accepted 22 February 2021; published 8 March 2021)

Hole spins in semiconductors are a potential qubit alternative to electron spins. In nuclear-spin-rich host crystals like GaAs, the hyperfine interaction of hole spins with nuclei is considerably weaker than that for electrons, leading to potentially longer dephasing times. Here we demonstrate optical pumping and coherent population trapping for acceptor-bound holes in a strained GaAs epitaxial layer. We find μs -scale longitudinal spin relaxation time T_1 and an inhomogeneous dephasing time T_2^* of ~ 7 ns. We attribute the spin relaxation mechanism to the combined effect of a hole-phonon interaction through the deformation potentials, and heavy-hole–light-hole mixing in an in-plane magnetic field. We attribute the short T_2^* to g -factor broadening due to strain inhomogeneity. T_1 and T_2^* are calculated based on these mechanisms and compared with the experimental results. While the hyperfine-mediated decoherence is mitigated, our results highlight the important contribution of strain to relaxation and dephasing of acceptor-bound hole spins.

DOI: [10.1103/PhysRevB.103.115412](https://doi.org/10.1103/PhysRevB.103.115412)**I. INTRODUCTION**

Spin systems in semiconductors have been actively studied due to the potential applications for nanoscale spintronics and quantum information technologies. Significant effort has been focused on electron spins in low-dimensional systems, e.g., quantum dots and donors [1–3]. However, due to the hyperfine interaction with the nuclei in the host crystal, the inhomogeneous dephasing time of electron spins can be short, typically on the nanosecond scale. Isotopic purification can significantly reduce this effect in group-IV and group II-VI semiconductors, e.g., in diamond and silicon. For group III-V semiconductors such as GaAs, this technique is not applicable as there is no stable isotope with zero nuclear spins. An alternative solution is to use hole spins, which have a much weaker hyperfine interaction due to the p -symmetry of the hole Bloch wave function [4]. Research in III-V quantum dots has shown μs -scale hole-spin dephasing times [5,6], compared to ns-scale in electron spins [7,8]. Spin control techniques such as optical pumping, coherent population trapping (CPT), and ultrafast optical control have been demonstrated [5,6,9]. Remote entanglement between two hole spins has been performed leveraging this enhanced dephasing time [10]. In addition to the enhanced coherence properties, faster electronic gate operations are possible due to large spin-orbit interaction, as demonstrated in silicon and germanium quantum dots [11,12].

A hole bound to an acceptor is a spin qubit system analogous to a hole-doped quantum dot with the added feature of high optical homogeneity [13]. However, because of the degeneracy of the heavy-hole (hh) and light-hole (lh) valence bands of GaAs, the strong spin-orbit interaction results in

a short spin relaxation time, typically much less than 1 ns [14,15]. This is not a problem in quantum dots as the mixing between hh and lh is significantly suppressed by the large hh-lh splitting due to strain and spatial confinement [16]. By analogy, if a large strain can be introduced to a p -doped GaAs crystal, relaxation times much longer than ns should also be achievable for hole spins bound to acceptors.

In this paper, we apply 0.04% compressive strain to a GaAs epitaxial layer, and we study the optical and spin properties of an ensemble of acceptors. We demonstrate optical pumping and CPT for the acceptor system in this strained GaAs sample. Microsecond-scale longitudinal hole spin relaxation time T_1 is observed. The measured magnetic-field dependence of T_1 can be explained by the combined effect of a hole-phonon interaction through the deformation potentials, and hh-lh mixing due to an in-plane magnetic field. An ~ 7 ns inhomogeneous dephasing time T_2^* is extracted from the CPT measurements. This time is much shorter than the measured >100 ns T_2^* for single hole spins in III-V quantum dots, determined by similar CPT measurements [5,6]. We attribute the short T_2^* to hole g -factor broadening due to strain inhomogeneity in the ensemble. We theoretically calculate the intrinsic T_2^* from the hyperfine interaction with nuclei to be around 60 ns.

The paper is organized as follows. Section II gives a brief description of the strained sample and the experimental setup. In Sec. III, we analyze the photoluminescence (PL) properties from acceptors, and we show how we calculate the strain from the PL spectra. In Secs. IV and V, we show the measurement techniques and the measured results for T_1 and T_2^* . The mechanisms of T_1 and T_2^* are briefly discussed in these

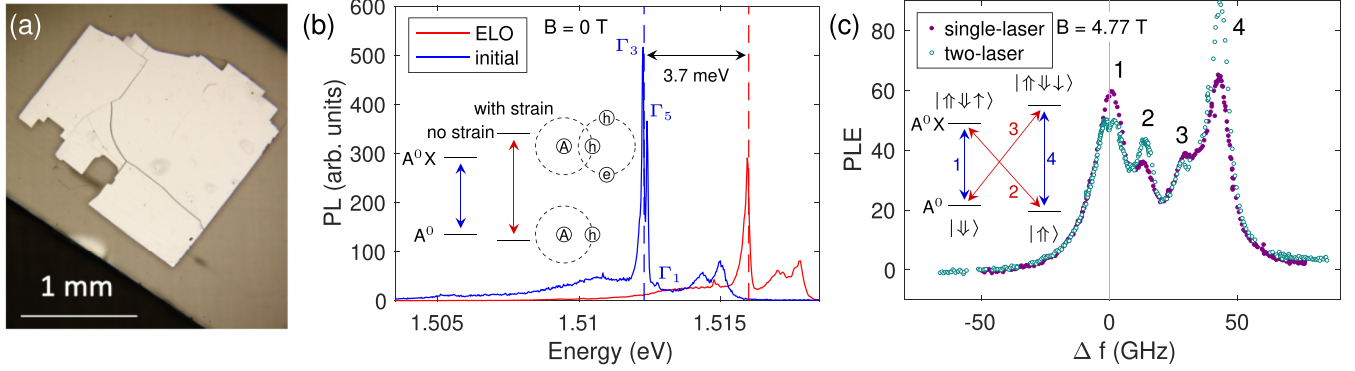


FIG. 1. (a) Optical microscope image of the GaAs epitaxial layer transferred to the MgO substrate. (b) PL spectra of the GaAs epitaxial layer before and after the ELO process at 1.5 K and 0 T. Excitation at 1.653 eV with 80 nW power. The laser spot diameter is $\sim 1 \mu\text{m}$. The inset shows the illustrated model of the acceptor systems and how the energies of A^0 and A^0X change with strain. In the illustrated diagram, “A” denotes the acceptor center, “h” denotes hole, and “e” denotes electron. (c) Single-laser and two-laser PLE spectra at 1.5 K and 4.77 T. The single-laser PLE spectrum is taken by scanning a laser across all four transitions and collecting the signal from two-hole transitions (THT). A typical THT spectrum is shown in Appendix B. The two-laser PLE spectrum is taken with a second laser fixed at the energy of transition 1. Δf is the detuning of the scanning laser with respect to the energy of transition 1. We have used background subtraction on both the single-laser and two-laser PLE spectra, where we use the PLE intensity at large Δf as the background. All lasers are at $1 \mu\text{W}$ power and 45° polarization. The laser spot diameter is $\sim 1 \mu\text{m}$. The inset shows the energy structure of the acceptor system. Transitions 1 and 4 (2 and 3) are polarized in the horizontal (vertical) direction.

two sections. In Sec. VI, we present detailed theory on the calculation of T_1 . The paper ends with a brief conclusion in Sec. VII.

II. SAMPLE DESCRIPTION AND EXPERIMENTAL SETUP

The strained sample consists of a $2 \mu\text{m}$ (001) *p*-type GaAs epitaxial layer on a MgO substrate. The GaAs layer is doped with carbon with an acceptor density of $\sim 2.5 \times 10^{14} \text{ cm}^{-3}$, determined from Hall measurements. Estimations show that at such a doping level, the overlap between neighboring acceptor wave functions is vanishingly small, so that acceptors are almost completely isolated from each other. The GaAs is transferred and bonded to the MgO substrate through an epitaxial lift-off (ELO) process at room temperature (see Appendix A). Compressive strain is introduced to GaAs when the sample is cooled down to 1.5 K due to the different thermal expansion rate of GaAs and MgO. The MgO substrate is chosen as the carrier as it is transparent at the band gap of GaAs and it can produce significant compressive strain. An optical microscope image of the transferred GaAs epitaxial layer on MgO is shown in Fig. 1(a). We note that this ELO method is not ideal; some cracking is observed, and possible slippage between the membrane and substrate can result in both strain reduction and strain inhomogeneity.

The photoluminescence (PL) of the sample is studied using a home-built confocal microscope with a resolution of $\sim 1 \mu\text{m}$. The sample is cooled to 1.5 K in a helium-immersion magnetic cryostat (Janis SOM). The hole spin states are controlled and measured with two tunable continuous-wave Ti:sapphire lasers (Spectra-Physics Matisse and Coherent 899-21). In pulsed experiments, the laser pulse is generated by passing the laser through an acousto-optic modulator (Gooch and Housego) with an on/off extinction ratio $> 10^4$.

III. INDUCED STRAIN AND PHOTOLUMINESCENCE PROPERTIES

Figure 1(b) shows the PL spectra before and after ELO at 0 T and 1.5 K. The main sharp peaks are from the transitions between the acceptor bound exciton (A^0X) and the neutral acceptor (A^0) states. The A^0 contains a single hole bound to the acceptor center. The A^0X contains two holes and an electron, similar to a positively charged trion. In the unstrained sample, three acceptor peaks— Γ_3 , Γ_5 , and Γ_1 —are observed due to the different hh and lh states for the two holes in A^0X , with the energy splitting due to hole-hole coupling and the crystal field [13]. As compressive strain introduces hh-lh splitting and a hh-like ground state, the two holes in A^0X are in the hh spin-singlet state, which corresponds to the single acceptor peak in the PL spectrum of the strained sample. Compared with the unstrained sample, an $\sim 3.7 \text{ meV}$ blueshift of the acceptor transition is observed. This energy shift is mainly caused by the shift of conduction and valence bands under strain, and it can be used as an estimate for the change in band-gap energy. The strain is estimated from the energy shift by $\Delta E = 2(a_c - a_v)(1 - C_{12}/C_{11})u_{xx}$, where a_c and a_v are the deformation potentials that determine the conduction- and valence-band shift, and C_{ij} are the components of the elastic stiffness tensor in GaAs; see Table I. From this, we obtain the value of the in-plane strain in our sample, $u_{xx} \approx u_{yy} \sim -0.04\%$. This strain leads to the splitting of the heavy- and light-hole subbands $E_{hh} - E_{lh} = 2b(1 + 2C_{12}/C_{11})u_{xx}$, where

TABLE I. Parameters used to calculate the strain and hh-lh splitting in the ELO [17].

a_c (eV)	a_v (eV)	C_{12}/C_{11}	b (eV)
-7.17	1.16	0.4526	-1.7

b is the valence-band deformation potential that determines the hh-lh splitting. We find $E_{hh} - E_{lh} \sim 2.6$ meV for GaAs parameters [18]. Since the splitting is positive for compressive strain, and it is much larger than the 0.13 meV thermal energy at 1.5 K, the majority of the holes populate the hh-like state. We note that the PL spectra are not homogeneous across the sample due to imperfect bonding during the ELO process. The spectrum selected after ELO in Fig. 1(b) is taken in a spot exhibiting relatively narrow transition lines. However, there is still a slight PL broadening compared to the as-grown sample.

The strained sample is studied in an in-plane magnetic field ($\vec{B} \perp [001]$). As shown in the inset of Fig. 1(c), there are four allowed optical transitions: transition 1 ($|\downarrow\rangle \leftrightarrow |\uparrow\downarrow\uparrow\rangle$), transition 2 ($|\uparrow\rangle \leftrightarrow |\uparrow\downarrow\uparrow\rangle$), transition 3 ($|\downarrow\rangle \leftrightarrow |\uparrow\downarrow\downarrow\rangle$), and transition 4 ($|\uparrow\rangle \leftrightarrow |\uparrow\downarrow\downarrow\rangle$). Here, $|\uparrow\rangle$ ($|\downarrow\rangle$) and $|\uparrow\downarrow\rangle$ ($|\downarrow\downarrow\rangle$) denote the eigenstates of the electron and hole in the in-plane field. The splitting between states $|\uparrow\rangle$ and $|\downarrow\rangle$ is due to the hole Zeeman splitting. The splitting between states $|\uparrow\downarrow\uparrow\rangle$ and $|\uparrow\downarrow\downarrow\rangle$ is due to the electron Zeeman splitting, as the two holes are in a spin singlet state. As shown by the PL spectra in Appendix C, transitions 1 and 4 are horizontally polarized (parallel to the magnetic field), while transitions 2 and 3 are vertically polarized (perpendicular to the magnetic field). The selection rules (Appendix D), together with the reasonable assumption $g_e^\perp < 0$ for the electron g -factor, yield $g_{hh}^\perp < 0$. The measured electron and hole g -factors are thus $g_e^\perp = -0.43$ and $g_{hh}^\perp = -0.15$.

A single-laser photoluminescence excitation (PLE) spectrum is taken to resolve all four transitions, as shown in Fig. 1(c). The single-laser PLE spectrum is taken by scanning a laser across the A^0X transitions and collecting the signal from the two-hole transitions (THT). To excite all four transitions, the laser is linearly polarized at 45° with respect to the magnetic field. From the spectrum, the inhomogeneous linewidth of the acceptor transitions is ~ 10 GHz. A two-laser PLE spectrum is taken to confirm the validity of the energy diagram shown in the inset of Fig. 1(c). In the two-laser PLE spectrum, one laser is fixed at transition 1 and a second laser is scanned across all four transitions. Compared to the single-laser PLE, there is a decrease in signals from transitions 1 and 3, and an enhancement of transitions 2 and 4. These changes are consistent with the effect of optical pumping in which the fixed laser pumps the spin states from $|\downarrow\rangle$ to $|\uparrow\rangle$ through the $|\uparrow\downarrow\uparrow\rangle$ state. Signals from transitions 1 and 3 (2 and 4) decrease (increase) as the intensity of these two transitions is proportional to the population in $|\downarrow\rangle$ ($|\uparrow\rangle$). Additionally, a small dip in peak 1 is observed, which is attributed to spectral hole burning. A fit of the dip shows a linewidth of ~ 1 GHz. Assuming it is transform-limited, it corresponds to a radiative lifetime of $1/(2\pi \times 1 \text{ GHz}) \simeq 0.2$ ns, which is in reasonable agreement with previous experimental measurements [13]. A small dip in peak 2 is expected due to CPT, which will be further discussed in Sec. V. However, due to the scan resolution, the CPT dip is not clearly resolved in this spectrum.

IV. OPTICAL PUMPING AND T_1 MEASUREMENT

In the $A^0 \leftrightarrow A^0X$ system, the A^0 holes can be initialized to a certain spin state by optical pumping. As shown in Fig. 2(a), a $5 \mu\text{s}$ laser pulse is applied resonantly on transition 1 so

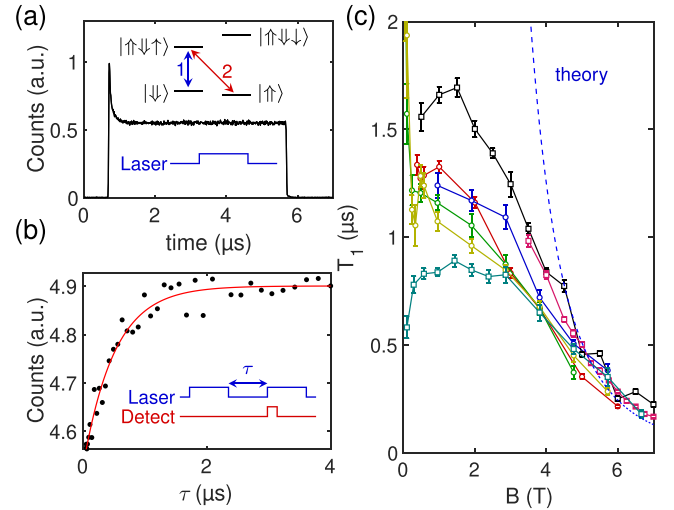


FIG. 2. (a) An optical pumping curve at 1.5 K and 1.9 T. The frequency of the laser is set on resonance with transition 1, and the laser power is 45 nW. The PL from transition 2 is collected with a single photon counting module. The laser spot diameter is $\sim 1 \mu\text{m}$. The insets show the energy diagram and the laser sequence. The detection is on all the time during the laser sequence. (b) A population recovery curve at 1.5 K and 1.9 T. The energy of the laser and detection are the same as in (a). A single exponential curve is used to fit for the T_1 . $T_1 = 0.51 \pm 0.04 \mu\text{s}$ for these data. The inset shows the laser sequence. The detection window is $0.8 \mu\text{s}$. (c) T_1 as a function of the magnetic fields. Different colors represent different locations on the sample. The dashed line shows the curve from theoretical calculation, Eq. (12).

the spin states are pumped from spin $|\downarrow\rangle$ to spin $|\uparrow\rangle$ through the $|\uparrow\downarrow\uparrow\rangle$ state. The PL signal from transition 2, which is proportional to the population of $|\downarrow\rangle$, is recorded during the optical pumping pulse. A decrease of the spin population is observed, indicating that partial spin initialization is achieved.

The spin relaxation time T_1 is measured by initializing the spin to $|\uparrow\rangle$ and measuring the recovery of the PL from transition 2 as a function of variable time τ . A single exponential fit is used to extract T_1 from the recovery curve, as shown in Fig. 2(b). T_1 as a function of magnetic field at different spots on the sample is shown in Fig. 2(c). Between 5 and 7 T, the magnitude of T_1 is similar at different spots on the sample, and the field dependence can be roughly approximated by $B^{-\nu}$ with $\nu \approx 3$ to 4. The accuracy of the estimate is limited by the small field range. At these high fields, we attribute the spin relaxation of holes to the admixture mechanism resulting from the hh-lh mixing by magnetic field and a hole-phonon interaction through the deformation potentials. The detailed theory is discussed in Sec. VI. The calculation based on this theory matches the experimental result, as shown in Fig. 2(c) by the dashed curve. Longer T_1 can potentially be achieved in the acceptor system by applying stronger and more homogeneous strain, which could be realized with other strain engineering techniques such as wafer bonding [19] or using piezoelectric actuators [20].

Below 5 T, T_1 is noticeably different at different locations on the sample, and it does not have a clear B -field dependence. A possible mechanism to explain this behavior is a

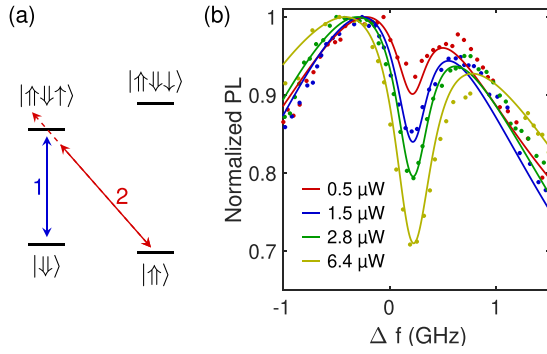


FIG. 3. (a) Energy diagram of the CPT experiment. The frequency of the control laser is fixed at transition 1 and the frequency of the probe laser is scanned across transition 2. (b) CPT with different probe laser power. Each curve is a two-laser PLE spectrum where Δf is the detuning of the probe laser compared to the energy of transition 2. The solid curves are from a simultaneous fit of the data at all different probe laser powers using the three-level density matrix model. The frequency of the control laser is fixed at transition 1 with a slight detuning of about 0.2 GHz, and the power is $3 \mu\text{W}$. The polarization of both lasers is set at 45° . The laser spot diameter is $\sim 1 \mu\text{m}$. The temperature is 1.5 K and the magnetic field is 7 T. We note that we have used background subtraction on all CPT curves where we use the signal at large Δf as the background.

combination of a hole-hole exchange interaction and inhomogeneous hyperfine fields, which is shown to be a mechanism for T_1 of donors at low fields [21]. This interaction depends on the local environment, such as the acceptor density, which can vary across the sample.

V. COHERENT POPULATION TRAPPING AND THE SPIN DEPHASING TIME T_2^*

Next, we perform coherent population trapping (CPT) on the A^0 - A^0X system to investigate the hole-spin coherence properties. As shown in Fig. 3(a), the A^0X state $|\uparrow\downarrow\uparrow\rangle$, together with the two A^0 states, $|\uparrow\rangle$ and $|\downarrow\rangle$, form a Λ -system. With a control laser driving the transition 1 ($|\downarrow\rangle \leftrightarrow |\uparrow\downarrow\uparrow\rangle$) and a probe laser driving the transition 2 ($|\uparrow\rangle \leftrightarrow |\uparrow\downarrow\uparrow\rangle$), a destructive interference occurs when the energy difference between the two lasers equals the hole Zeeman splitting. On the two-photon resonance, the system is pumped into a dark state, i.e., a superposition state between $|\uparrow\rangle$ and $|\downarrow\rangle$ [22,23].

In our experiment, CPT is revealed by the two-laser PLE spectrum. The energy of the control laser is fixed near the resonance of transition 1, and the probe laser is scanned across the transition 2. A dip in the PLE spectrum occurs at the two-photon resonance, as shown in Fig. 3(b). The linewidth and depth of the dip depend on the laser powers, the spontaneous emission rate of the $|\uparrow\downarrow\uparrow\rangle$ state, and the dephasing rate between $|\uparrow\rangle$ and $|\downarrow\rangle$. The CPT phenomenon is simulated by solving the master equation of a three-level density matrix considering all relaxation and dephasing terms (see Appendix E).

In Fig. 3, the CPT curves at different probe powers are simultaneously fit with the density matrix model. The inhomogeneous dephasing time T_2^* between the two spin states is found to be ~ 7 ns. The measured T_2^* in our sample is

significantly smaller than the > 100 ns T_2^* measured in single III-V quantum dots [5,6]. We attribute the short T_2^* to g -factor broadening due to strain inhomogeneity in the sample. The 7 ns T_2^* corresponds to a Gaussian broadening of the in-plane hole g -factor ($g_{\text{hh}}^\perp = -0.15$) with a standard deviation of 0.0003. This g -factor broadening introduces inhomogeneity to the spin splitting between $|\uparrow\rangle$ and $|\downarrow\rangle$, and hence to the spin precession frequency, which leads to a stronger dephasing. We note that T_2^* depends on the local strain environment, and we have measured T_2^* ranging from 4 to 8 ns on the sample. In Appendix F, we calculate the intrinsic spin dephasing time due to dipole-dipole hyperfine interaction to be $T_2^* \approx 58$ ns. This longer dephasing time could be achieved by using strain engineering techniques that provide more homogeneous strain.

VI. THEORY OF THE HEAVY-HOLE LONGITUDINAL SPIN RELAXATION TIME T_1

A. Wave functions of acceptor-bound holes

The acceptor-bound hole states in cubic semiconductors are determined by an interplay of the spin-orbit interaction and the Coulomb energy. Before calculating the spin relaxation times, we establish the form of the hole wave functions and Zeeman effect in the studied system where strain is present.

In the spherical approximation, the hole bound to an acceptor is described by the total angular momentum F , which is the sum of the free-hole angular momentum J ($J = 3/2$ originating from the valence-band Bloch functions) and the orbital momentum L of the hole moving in the Coulomb field of an acceptor. In the ground state of the hole, $F = 3/2$ and $L = 0, 2$ [24,25]. In the absence of external fields, this state is fourfold degenerate with respect to the projection of the total angular momentum F_z . The corresponding wave functions $|F_z\rangle$ are [24,25]

$$\begin{aligned}
 |\pm 3/2\rangle &= \left[f(r)Y_0^0(\theta, \varphi) + \frac{g(r)}{\sqrt{5}}Y_2^0(\theta, \varphi) \right] |J, \pm 3/2\rangle \\
 &\quad - \sqrt{\frac{2}{5}}g(r)[Y_2^{\pm 1}(\theta, \varphi)|J, \pm 1/2\rangle \\
 &\quad - Y_2^{\pm 2}(\theta, \varphi)|J, \mp 1/2\rangle], \\
 |\pm 1/2\rangle &= \left[f(r)Y_0^0(\theta, \varphi) - \frac{g(r)}{\sqrt{5}}Y_2^0(\theta, \varphi) \right] |J, \pm 1/2\rangle \\
 &\quad + \sqrt{\frac{2}{5}}g(r)[Y_2^{\mp 1}(\theta, \varphi)|J, \pm 3/2\rangle \\
 &\quad + Y_2^{\pm 2}(\theta, \varphi)|J, \mp 3/2\rangle], \quad (1)
 \end{aligned}$$

where $Y_m^l(\theta, \varphi)$ are the spherical harmonic functions, $f(r)$ and $g(r)$ are the radial parts of the envelope functions, and $|J, J_z\rangle$ are the Bloch functions of the Γ_8 band.

Now let us consider the effect of strain and magnetic field on the ground acceptor state. The biaxial strain induces the splitting between $|\pm 3/2\rangle$ and $|\pm 1/2\rangle$ states discussed in Sec. III. Since the estimated value of this splitting (~ 2.6 meV) is much smaller than the hole binding energy (~ 25 meV) [13,24], it is possible to neglect the coupling of the ground acceptor state to the excited ones and consider the quadruplet

(1) only. In the presence of strain and magnetic field $\mathbf{B} \parallel x$, the Hamiltonian describing the ground state of an acceptor-bound hole in the basis [Eq. (1)] reads

$$\mathcal{H}_0 = -\frac{\Delta_0}{2}F_z^2 + g_0\mu_BBF_x. \quad (2)$$

Here $\Delta_0 > 0$ is the strain-induced splitting between $|\pm 3/2\rangle$ and $|\pm 1/2\rangle$ doublets, g_0 is the g -factor of an acceptor-bound hole in the absence of strain (accounting for the Coulomb effects) [26,27], F_j are the matrices of the angular momentum $F = 3/2$, and μ_B is the Bohr magneton.

The Hamiltonian (2) does not yield linear in B splitting of the $|\pm 3/2\rangle$ doublet, observed in the experiment (see Sec. III), and it is insufficient to describe the experimental data. A nonzero heavy-hole in-plane g -factor g_{hh}^\perp results from cubic symmetry terms $\sum_\alpha F_\alpha^3 B_\alpha$ allowed in zinc-blende semiconductors, however these terms are small since they originate from the coupling with remote electronic bands [28]. Larger values of g_{hh}^\perp result from the presence of anisotropic in-plane strain, i.e., nonzero u_{xy} or $u_{xx} - u_{yy}$ components of the strain tensor, in our sample. This anisotropic strain might be attributed to imperfect bonding between the GaAs epitaxial layer and the MgO substrate. The experimentally observed selection rules are consistent with $|u_{xx} - u_{yy}| \gg |u_{xy}|$ (Appendix D), and therefore we consider the case $u_{xx} \neq u_{yy}$, $u_{xy} = 0$ in the following. In this case, the hole Hamiltonian has the form

$$\mathcal{H} = \mathcal{H}_0 + \frac{\Delta_1}{2}(F_x^2 - F_y^2), \quad (3)$$

where the additional term $\propto \Delta_1 \propto u_{xx} - u_{yy}$ accounts for the anisotropic in-plane strain in the sample. Due to the same reason (small u_{xy}), we do not take into account piezoelectric fields in the sample, which might also affect the hole states.

The Hamiltonian (3) couples the $|\pm 3/2\rangle$ states resulting in the splitting of the doublet. As a result, the new states $|\uparrow\rangle$ and $|\downarrow\rangle$ with energies $\varepsilon_{\uparrow,\downarrow} = -9\Delta_0/8 \pm g_{hh}^\perp\mu_B B/2$ are formed. At $|\Delta_1|, |g_0\mu_B B| \ll \Delta_0$, relevant to experimental conditions, the corresponding transverse g -factor and wave functions of the heavy-hole states are

$$g_{hh}^\perp = -\frac{3\Delta_1}{\Delta_0}g_0, \quad (4)$$

$$\begin{aligned} |\uparrow\rangle &= \frac{1}{\sqrt{2}} \left[| +3/2 \rangle - \frac{\sqrt{3}}{2\Delta_0} (\Delta_1 + g_0\mu_B B) | +1/2 \rangle \right. \\ &\quad \left. - \frac{\sqrt{3}}{2\Delta_0} (\Delta_1 + g_0\mu_B B) | -1/2 \rangle + | -3/2 \rangle \right], \\ |\downarrow\rangle &= \frac{1}{\sqrt{2}} \left[| +3/2 \rangle + \frac{\sqrt{3}}{2\Delta_0} (\Delta_1 - g_0\mu_B B) | +1/2 \rangle \right. \\ &\quad \left. - \frac{\sqrt{3}}{2\Delta_0} (\Delta_1 - g_0\mu_B B) | -1/2 \rangle - | -3/2 \rangle \right]. \end{aligned} \quad (5)$$

We stress that in Eqs. (4) and (5), the Zeeman energy $g_0\mu_B B$ and the strain-induced coupling parameter Δ_1 can be comparable in magnitude.

It follows from Eq. (5) that optical transitions $|\downarrow\rangle \leftrightarrow |\uparrow\downarrow\uparrow\rangle$ and $|\uparrow\rangle \leftrightarrow |\uparrow\downarrow\downarrow\rangle$ are active in x -polarization, whereas transitions $|\uparrow\rangle \leftrightarrow |\uparrow\downarrow\uparrow\rangle$ and $|\downarrow\rangle \leftrightarrow |\uparrow\downarrow\downarrow\rangle$ are active in

y -polarization (see Appendix D for details). By comparison with Fig. 1(c), we conclude that $\varepsilon_\downarrow > \varepsilon_\uparrow$, and hence $g_{hh}^\perp < 0$.

B. The rate of spin-flip transitions

Similarly to the case of localized electrons [4], the spin-flip transitions between the bound hole states in a sufficiently strong magnetic field, where the Zeeman splitting exceeds by far the hyperfine coupling, are controlled by the hole-phonon interaction. An important difference, however, is that the electron spin flip is a second-order process and also requires spin-dependent terms in the conduction band (e.g., Dresselhaus k^3 spin splitting), which are present in noncentrosymmetric media only, whereas the hole spin flip is efficient already in the isotropic approximation. In moderate magnetic fields studied here, the transitions are mediated by acoustic phonons, which can give or take Zeeman energy in the course of spin relaxation. The interaction of Zeeman sublevels with an acoustic phonon is possible since the heavy-hole states $|\uparrow\rangle$ ($|\downarrow\rangle$) have an admixture of light holes in the presence of magnetic field, as follows from Eq. (5). Hence, these states are coupled under phonon-induced deformation through the Bir-Pikus Hamiltonian [29]. Here the complex valence-band structure facilitates direct spin-phonon interaction.

The spin-flip transition rates are found using Fermi's golden rule, e.g., the rate of a $|\uparrow\rangle \rightarrow |\downarrow\rangle$ transition with emission of a phonon is

$$\Gamma_{\downarrow\uparrow} = \frac{2\pi}{\hbar} \sum_{q,\alpha} |M_{\downarrow\uparrow}|^2 \delta(\hbar q s_\alpha - |g_{hh}^\perp \mu_B B|), \quad (6)$$

where $M_{\downarrow\uparrow}$ is the spin-flip matrix element, \mathbf{q} is the phonon wave vector, and s_α is the speed of sound in the phonon branch α . The spin-flip matrix element is $M_{\downarrow\uparrow} = \langle \downarrow | \mathcal{H}_{BP} | \uparrow \rangle$, where \mathcal{H}_{BP} is the Bir-Pikus Hamiltonian [30], which in the basis (1) reads

$$\begin{aligned} \mathcal{H}_{BP} &= \left(a' + \frac{5}{4} b' \right) \sum_i u_{ii} - b' \sum_i F_i^2 u_{ii} \\ &\quad - \frac{d'}{\sqrt{3}} \sum_{i \neq i'} \{ F_i F_{i'} \} u_{i'i}. \end{aligned} \quad (7)$$

Here a' , b' , and d' are the valence-band deformation potentials modified by the Coulomb interaction, $b'/b = d'/d = \int dr r^2 [f^2(r) - 3g^2(r)/5]$ [31]. The phonon-induced deformation results in the strain components

$$u_{ij}^{q,\alpha} = \sqrt{\frac{\hbar}{2\rho\omega_{q,\alpha}}} \frac{i[q_i e_j^{(q,\alpha)} + q_j e_i^{(q,\alpha)}]}{2} e^{i(\mathbf{q}\cdot\mathbf{r} - \omega_{q,\alpha}t)} b_{q,\alpha}^\dagger + \text{c.c.}, \quad (8)$$

where $\mathbf{e}^{(q,\alpha)}$ is the polarization vector, ω is the phonon frequency, ρ is the mass density, and $b_{q,\alpha}^\dagger$ is the phonon creation operator. For LA phonons, $\mathbf{e}^{(1)} = (q_x, q_y, q_z)/q$, whereas for TA phonons, there are two modes with $\mathbf{e}^{(2)} = (q_y, -q_x, 0)/q_\perp$ and $\mathbf{e}^{(3)} = (q_x q_z, q_y q_z, -q_\perp^2)/q q_\perp$, where $q_\perp = \sqrt{q_x^2 + q_y^2}$. Furthermore, we use the long-wavelength approximation for the phonons, i.e., $e^{i\mathbf{q}\cdot\mathbf{r}} \approx 1$.

TABLE II. Parameters used to calculate T_1 . Parameter $|g_{\text{hh}}^{\perp}|$ is determined from PL experiments; see Sec. III.

ρ (kg/m ³)	s_l (m/s)	s_r (m/s)	$ g_{\text{hh}}^{\perp} $
5.32×10^3 [21]	4.73×10^3 [21]	3.35×10^3 [21]	0.15

At zero temperature (when no phonons are present) it follows from Eqs. (5), (7), and (8) that

$$M_{\downarrow\uparrow} = \frac{3g_0\mu_B B b'}{2\Delta_0} \sqrt{\frac{\hbar}{2\rho\omega}} (iq_x e_z + iq_z e_x + q_x e_y + q_y e_x), \quad (9)$$

where for simplicity we used the spherical approximation $b' = d'/\sqrt{3}$ for the Bir-Pikus Hamiltonian. Note that in agreement with time-reversal symmetry, the spin-flip matrix-element is proportional to B , so that only magnetic-field-induced admixture of light holes in the states (5) is relevant for the spin-flip process. The spin-flip rate calculated after Eqs. (6) and (9) is

$$\Gamma_{\downarrow\uparrow} = \frac{(g_{\text{hh}}^{\perp}\mu_B B)^5}{10\pi\rho\hbar^4(u_{xx} - u_{yy})^2} \left(\frac{1}{s_r^5} + \frac{2}{3s_l^5} \right), \quad (10)$$

where we used Eq. (4) to exclude unknown parameter g_0 and the relation $\Delta_1 = -b'(u_{xx} - u_{yy})$.

The measured spin relaxation time T_1 at nonzero temperature is given by

$$T_1 = \frac{1}{\Gamma_{\downarrow\uparrow}(T) + \Gamma_{\uparrow\downarrow}(T)}, \quad (11)$$

where $\Gamma_{\uparrow\downarrow}(T) = \Gamma_{\downarrow\uparrow}[N_{\text{ph}}(T) + 1]$, $\Gamma_{\downarrow\uparrow}(T) = \Gamma_{\uparrow\downarrow}N_{\text{ph}}(T)$, and $N_{\text{ph}}(T)$ is the phonon occupation number. Using an explicit expression for $N_{\text{ph}}(T)$, we find

$$T_1 = \frac{e^{\beta} - 1}{\Gamma_{\downarrow\uparrow}(e^{\beta} + 1)}, \quad (12)$$

where $\beta = |g_{\text{hh}}^{\perp}\mu_B B|/k_B T$, and $k_B T$ is the thermal energy. In the whole range of applied magnetic fields, $\beta \ll 1$, and hence $T_1 = \beta/(2\Gamma_{\downarrow\uparrow}) \propto B^{-4}$. The values of the parameters used to calculate T_1 are listed in Table II. With $|u_{xx} - u_{yy}| = 0.008\%$, so that $|u_{xx} - u_{yy}|/|u_{xx}| = 0.2$, the theoretical T_1 curve agrees well with the measured data at high fields, shown in Fig. 2(c). It corresponds to $|\Delta_1|/\Delta_0 \approx 0.05$, and using the measured value of $|g_{\text{hh}}^{\perp}| = 0.15$ we estimate $|g_0| \approx 1$. This agrees with the values from the literature, which have reported hole g -factors ranging from 0.52 to 2.34 [27,32,33].

VII. CONCLUSION

We have introduced compressive strain into a p -type GaAs epitaxial layer through the epitaxial liftoff technique. This strain breaks the degeneracy of heavy- and light-hole states, leading to μs -scale longitudinal spin relaxation times T_1 of the heavy hole. Coherent population trapping measurements indicate a 7 ns hole spin dephasing time T_2^* in this strained sample. We quantitatively explain the measured T_1 and T_2^* values based on two different mechanisms. The measured T_1 is explained by a hole-phonon interaction mediated by heavy-hole–light-hole mixing in the in-plane magnetic

field, and the measured T_2^* is explained by in-plane hole g -factor broadening due to strain inhomogeneity. Other strain engineering techniques such as wafer bonding [19] or piezoelectric actuators [20] can possibly provide stronger and more homogeneous strain in the sample, which can potentially enhance both T_1 and T_2^* in the acceptor-hole system.

ACKNOWLEDGMENTS

This material is based upon work supported by the National Science Foundation under Grants No. 1150647 and No. 1820614. M.V.D. acknowledges financial support from the Basis Foundation for the Advancement of Theoretical Physics and Mathematics. M.M.G. was partially supported by the Saint-Petersburg State University for a research Grant No. 51125686. M.V.D. and M.M.G. were partially supported by RFBR and CNRS according to the research Project No. 20-51-16303.

APPENDIX A: ELO PROCESS

In the strained sample, the GaAs epitaxial layer is transferred to the MgO substrate through an ELO technique. The as-grown GaAs sample contains a $2\ \mu\text{m}$ p -type GaAs epitaxial layer with $\sim 50\ \text{nm}$ $\text{Al}_{0.2}\text{Ga}_{0.8}\text{As}$ cladding and an $100\ \text{nm}$ AlAs sacrificial layer for ELO, with all those layers on a GaAs substrate. The AlAs sacrificial layer is selectively etched in 5% hydrofluoric acid for $\sim 24\ \text{h}$ to release the $2\ \mu\text{m}$ GaAs epitaxial layer from the GaAs substrate. An $\sim 1\text{-mm}$ -thick photoresist layer is applied to the membrane before the etching for protection. The photoresist needs to be mm thick so the GaAs epitaxial layer can bend with a small angle to let the acid etch in. After the etching, the membrane is transferred to a beaker with water for cleaning and then to an MgO substrate. A thin paper tissue is used to wick the water out from between the epitaxial layer and the MgO substrate. The sample is then put in a SPI membrane box to add pressure on top of the GaAs epitaxial layer to improve bonding with the new substrate. After waiting for ~ 3 days, the sample is taken out and the photoresist on top of the epitaxial layer is removed in hot solvent.

APPENDIX B: SPECTRUM OF THTs

The two-hole transitions (THTs) are the transitions from the A^0X to higher orbital states of A^0 . A^0 has a hydrogenlike wave function. The main acceptor transitions are from A^0X to $n = 1$ states of A^0 . The THTs are from A^0X to $n > 1$ states of A^0 , as shown in Fig. 4. For all the PLE spectra, we collect the signal from the $n = 2$ THTs.

APPENDIX C: IN-PLANE g -FACTORS

The absolute values of the measured in-plane hole and electron g -factors are $|g_{\text{hh}}^{\perp}| = 0.15 \pm 0.01$ and $|g_e^{\perp}| = 0.43 \pm 0.01$, as shown in Fig. 5(a). These values are close to the values measured in InGaAs/GaAs quantum dots [34]. The sign of both the electron and hole g -factors is negative, as discussed in Appendix D.

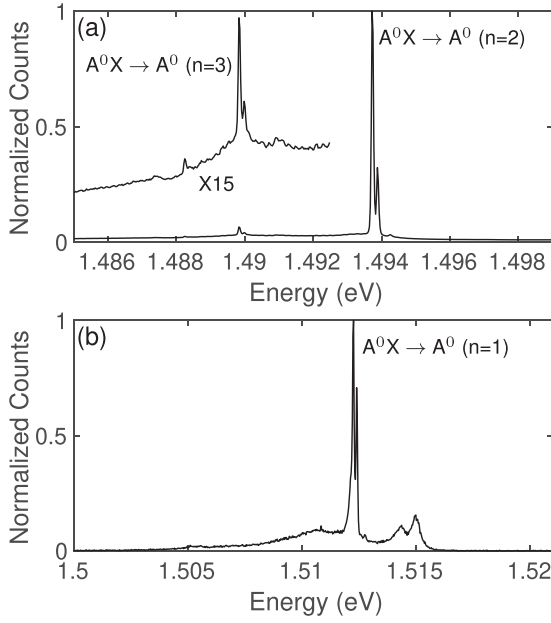


FIG. 4. (a) Spectrum of the $n = 2$ and 3 THTs. The excitation is on resonance with the acceptor transition at 1.512 eV and the power is at $0.9 \mu\text{W}$. The temperature is at 2 K and the magnetic field is at 0 T. (b) The corresponding spectrum of the main acceptor transitions. Excitation at 1.653 eV with 13 nW power. The laser has a spot size of $\sim 1 \mu\text{m}$. The spectra are taken in the sample before the ELO process.

APPENDIX D: SELECTION RULES

The selection rules are derived using a similar method to that in Ref. [3]. Note that in this Appendix, we consider a free heavy hole, not a hole bound to an acceptor, which is described by wave functions (1), and it contains also an admixture of light-hole states. However, since $g(r) \ll f(r)$, we can neglect the contribution of light holes to the optical transition matrix element. At zero magnetic field, the eigenfunctions for electrons are

$$\begin{aligned} |\uparrow\rangle_z &= |\uparrow_z, S\rangle, \\ |\downarrow\rangle_z &= |\downarrow_z, S\rangle, \end{aligned} \quad (\text{D1})$$

where $|S\rangle$ is the orbital Bloch function for electrons. The eigenfunctions for heavy holes are

$$\begin{aligned} |\uparrow\rangle_z &= -\left| \uparrow_z, \frac{X + iY}{\sqrt{2}} \right\rangle = | +3/2 \rangle, \\ |\downarrow\rangle_z &= \left| \downarrow_z, \frac{X - iY}{\sqrt{2}} \right\rangle = | -3/2 \rangle, \end{aligned} \quad (\text{D2})$$

where $\left| \frac{X \pm iY}{\sqrt{2}} \right\rangle$ is the orbital Bloch function for holes. In an in-plane magnetic field ($B \parallel x$), the electron states become

$$\begin{aligned} |\uparrow\rangle_x &= \frac{1}{\sqrt{2}}(|\uparrow\rangle_z + |\downarrow\rangle_z), \\ |\downarrow\rangle_x &= \frac{1}{\sqrt{2}}(|\uparrow\rangle_z - |\downarrow\rangle_z). \end{aligned} \quad (\text{D3})$$

The hole states in the in-plane field are determined by an interplay of the Zeeman effect and the strain. Assuming a nonzero $u_{xx} - u_{yy}$ and a zero u_{xy} , the hole states in a magnetic

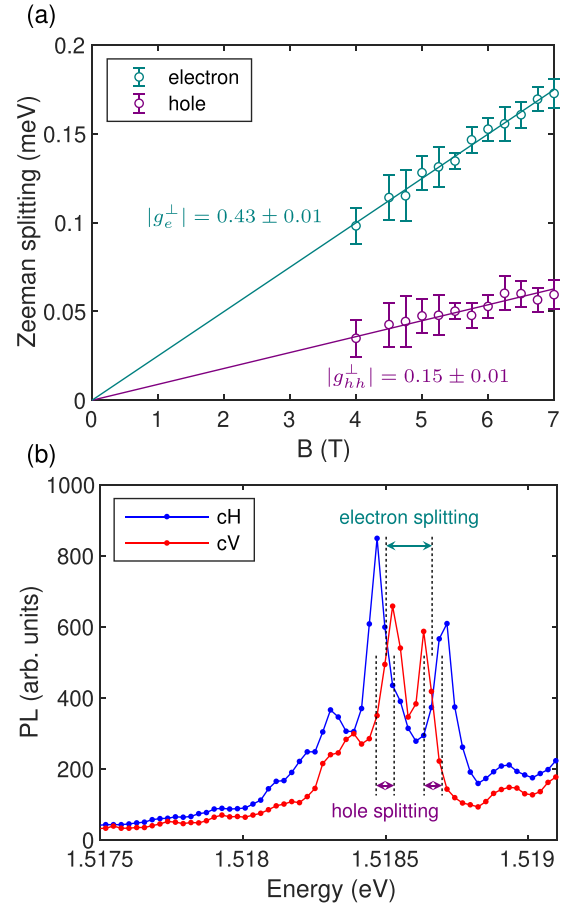


FIG. 5. (a) Electron and hole Zeeman splitting as a function of the in-plane magnetic field. (b) PL spectra with horizontal and vertical polarization in collection. The magnetic field is at 7 T and the temperature is at 1.5 K. Excitation at 1.53 eV with 200 nW power. The electron and hole splittings are marked in the spectra.

field become

$$\begin{aligned} |\uparrow\rangle_x &= \frac{1}{\sqrt{2}}(|\downarrow\rangle_z + |\uparrow\rangle_z) = \frac{1}{\sqrt{2}}(|-3/2\rangle + |+3/2\rangle), \\ |\downarrow\rangle_x &= \frac{1}{\sqrt{2}}(-|\downarrow\rangle_z + |\uparrow\rangle_z) = \frac{1}{\sqrt{2}}(|+3/2\rangle - |-3/2\rangle). \end{aligned} \quad (\text{D4})$$

Note that these wave functions coincide with Eq. (5) if one neglects the light-hole admixture. The dipole matrix element for the recombination of the electron state $|i\rangle$ and hole state $|j\rangle$ is $\mu_{ij} = \langle ij | \boldsymbol{\mu} | 0 \rangle$, where $|0\rangle$ is the ground state of a crystal, $\boldsymbol{\mu} = e\mathbf{r}$ is the dipole moment operator, e is the electron charge, and $\mathbf{r} = x\hat{x} + y\hat{y} + z\hat{z}$ is the position vector. The calculated results of the four μ_{ij} are shown below:

$$\begin{aligned} \langle \uparrow_x \uparrow_x | \boldsymbol{\mu} | 0 \rangle &= -\frac{\mu_0}{\sqrt{2}} \hat{x}, & \langle \uparrow_x \downarrow_x | \boldsymbol{\mu} | 0 \rangle &= -i\frac{\mu_0}{\sqrt{2}} \hat{y}, \\ \langle \downarrow_x \uparrow_x | \boldsymbol{\mu} | 0 \rangle &= i\frac{\mu_0}{\sqrt{2}} \hat{y}, & \langle \downarrow_x \downarrow_x | \boldsymbol{\mu} | 0 \rangle &= \frac{\mu_0}{\sqrt{2}} \hat{x}, \end{aligned} \quad (\text{D5})$$

where $\mu_0 = e\langle X|x|S\rangle = e\langle Y|y|S\rangle = e\langle Z|z|S\rangle$.

Now let us consider selection rules. Assume that the initial state is $|\downarrow\rangle_x$. Following from Eq. (D5), x -polarized radiation excites a $|\uparrow\rangle_x |\uparrow\rangle_x$ electron-hole pair. Hence we have the

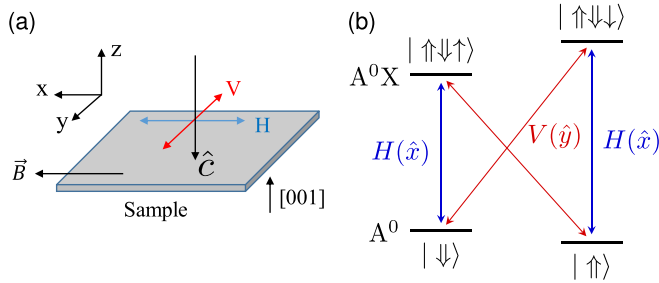


FIG. 6. (a) Geometry of the experiment. x (H) is the horizontal direction (parallel to the magnetic field \vec{B}) and y (V) is the vertical direction (perpendicular to the magnetic field \vec{B}). \hat{c} is the direction of the optical axis, which is parallel to the [001] axis of the GaAs epilayer. (b) Energy diagram and selection rules of the acceptor system under magnetic fields.

transition $|\downarrow\rangle_x \rightarrow |\uparrow_x\downarrow_x\uparrow_x\rangle$ for the x -polarized radiation, as shown in Fig. 6(b). Other selection rules are obtained in the same fashion. Note that in all the figures, the subscript “ x ” is ignored for simplicity. We also obtain that $|\downarrow\rangle$ has larger energy than $|\uparrow\rangle$ [following from the experimental spectra in Fig. 5(b)], therefore the hole g -factor is negative.

Similar to the analysis in Ref. [3], we only use single-particle wave functions for electrons and holes, and the exchange interaction is ignored. For A^0X , as the two holes are in a spin singlet state, the exchange interaction between the electron and hole should be weak [35]. From the PLE spectra in Fig. 1(c), no exchange splitting is observed within the 10 GHz inhomogeneous linewidth in our experiment.

$$L = \begin{pmatrix} -\Gamma_{12}\rho_{11} + \Gamma_{21}\rho_{22} + \Gamma_3\rho_{33} & -(\frac{\Gamma_{12}+\Gamma_{21}}{2} + \gamma_{12})\rho_{12} & -(\frac{\Gamma_{12}+2\Gamma_3}{2} + \gamma_3)\rho_{13} \\ -(\frac{\Gamma_{12}+\Gamma_{21}}{2} + \gamma_{12})\rho_{21} & \Gamma_{12}\rho_{11} - \Gamma_{21}\rho_{22} + \Gamma_3\rho_{33} & -(\frac{\Gamma_{21}+2\Gamma_3}{2} + \gamma_{33})\rho_{23} \\ -(\frac{\Gamma_{12}+2\Gamma_3}{2} + \gamma_3)\rho_{31} & -(\frac{\Gamma_{21}+2\Gamma_3}{2} + \gamma_3)\rho_{32} & -2\Gamma_3\rho_{33} \end{pmatrix}. \quad (\text{E2})$$

Γ_{12} (Γ_{21}) is the relaxation rate from $|\downarrow\rangle$ ($|\uparrow\rangle$) to $|\uparrow\rangle$ ($|\downarrow\rangle$). The spin relaxation time T_1 satisfies

$$\Gamma_{12} = \frac{1}{T_1} \frac{1}{1 + e^{-g\mu_B B/k_b T}}, \quad (\text{E3})$$

$$\Gamma_{21} = \frac{1}{T_1} \frac{e^{-g\mu_B B/k_b T}}{1 + e^{-g\mu_B B/k_b T}}, \quad (\text{E4})$$

where $g\mu_B B$ is the hole Zeeman splitting and $k_b T$ is the thermoenergy. $\gamma_{12} = 1/T_2$ is the dephasing rate between $|\uparrow\rangle$ and $|\downarrow\rangle$. Γ_3 and γ_3 are the spin relaxation rate and dephasing rate between the excited state $|\uparrow\downarrow\rangle$ and the ground spin states. For simplicity, we assume they are the same for $|\uparrow\rangle$ and $|\downarrow\rangle$. Δ_c and Ω_c are the detuning and strength of the control laser. Δ_p and Ω_p are the detuning and strength of the probe laser. The population of the excited state ρ_{33} after equilibrium is calculated as the final result, which is proportional to the detected PL intensity in the two-laser PLE experiment. All important fitting parameters and the fitting results are shown in Table III.

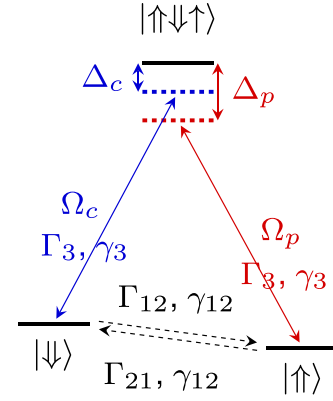


FIG. 7. Energy diagram of the Λ system.

APPENDIX E: DENSITY MATRIX MODEL FOR CPT

In our experiment, the states $|\uparrow\downarrow\rangle$, $|\uparrow\rangle$, and $|\downarrow\rangle$ are used to form the Λ system, as shown in Fig. 7. The evolution of the Λ system can be simulated by solving the master equation $\partial\rho/\partial t = -i[H, \rho] + L(\rho)$. In the equation, H is the Hamiltonian of the system,

$$H_i = -\hbar \begin{pmatrix} \Delta_c & 0 & \Omega_c^*/2 \\ 0 & \Delta_p & \Omega_p^*/2 \\ \Omega_c/2 & \Omega_p/2 & 0 \end{pmatrix} \begin{pmatrix} |\downarrow\rangle \\ |\uparrow\rangle \\ |\uparrow\downarrow\rangle \end{pmatrix}, \quad (\text{E1})$$

where Δ_p and Δ_c is the detuning of the probe and the control laser. L is the Lindblad operator including the relaxation and dephasing between different states,

APPENDIX F: THEORY OF THE INHOMOGENEOUS DEPHASING TIME T_2^* DUE TO HYPERFINE INTERACTION WITH NUCLEAR SPINS

The hole spin dephasing originates from the dipole-dipole part of the hyperfine interaction. In bulk semiconductors, it is given by the Hamiltonian acting on the four-component

TABLE III. Fitting parameters for the three-level density matrix model. The errors are 2σ errors from fitting.

Parameter	Fit values
T_2^* (ns)	6.8 ± 0.7
T_1 (μ s)	0.09 ± 0.01
Γ_3 (GHz)	0.63 ± 0.03
γ_3 (GHz)	0.64 ± 0.05
Ω^2/power ($\text{GHz}^2/\mu\text{W}$)	0.046 ± 0.004
Δ_{c0} (GHz)	0.215 ± 0.009

envelope function [4],

$$\mathcal{H}_{\text{hf}} = \sum_{j,a} \frac{A_a v_0}{2} \delta(\mathbf{r} - \mathbf{R}_{j,a}) (M_{1,a} \mathbf{I}^{j,a} \cdot \mathbf{J} + M_{2,a} \mathbf{I}^{j,a} \cdot \mathbf{J}^3), \quad (\text{F1})$$

where $a = \text{Ga, As}$ is the crystal sublattice index, j enumerates nuclei in a given sublattice, v_0 is the volume of the unit cell, $\mathbf{R}_{j,a}$ is the position of the j th nucleus in the sublattice a , A_a is the conduction-band hyperfine coupling constant, $\mathbf{I}^{j,a} = (I_x^{j,a}, I_y^{j,a}, I_z^{j,a})$ is the spin of the nucleus, we recall that \mathbf{J} is the free-hole angular momentum, and we use the notation $\mathbf{J}^3 = (J_x^3, J_y^3, J_z^3)$. In Eq. (F1), $M_{1,a}$ and $M_{2,a}$ are the dimensionless parameters with $M_{2,a}$ resulting from the cubic symmetry of the crystal. Depending on the material system and isotope in question, the parameters $M_{1,a}$ and $M_{2,a}$ can be comparable [4,36,37]. Hereafter, for simplicity, we take into account the contribution of $M_{1,a}$ only: As we see below, it already produces the right order of magnitude of the dephasing time.

In our experiments, the hole spin dephasing is studied in the Voigt configuration where $\mathbf{B} \parallel x$. In the external field along the x -axis, the hole states $|\uparrow\rangle$ and $|\downarrow\rangle$ are given by Eq. (5) with the $|\pm 3/2\rangle$ and $|\pm 1/2\rangle$ basis functions given by the general expressions (1). Provided that the field is sufficiently strong, i.e., under the conditions where the hole Zeeman splitting in the magnetic field, $|g_{\text{hh}}^\perp \mu_B B|$, Eq. (4), exceeds by far the splittings induced by the nuclear spin fluctuations, the dephasing is controlled by the nuclear field fluctuations in the directions of the hole pseudospin. We calculate $\Omega_{N,x}$, the contribution to Larmor frequency due to nuclei, as

$$\hbar \Omega_{N,x} = \langle \uparrow | \mathcal{H}_{\text{hf}} | \uparrow \rangle - \langle \downarrow | \mathcal{H}_{\text{hf}} | \downarrow \rangle. \quad (\text{F2})$$

The analysis shows that it contains B -independent and B^2 terms; the latter are neglected. Correspondingly, the mean-square fluctuation of the nuclear field is

$$\langle \Omega_{N,x}^2 \rangle = \frac{v_0^2 \sum_a C_a^2 I_a (I_a + 1)}{27 \hbar^2} \times \sum_j [j_x^2(\mathbf{R}_j) + j_y^2(\mathbf{R}_j) + j_z^2(\mathbf{R}_j)], \quad (\text{F3})$$

where $C_a = 3A_a M_{1,a}/2$ and $j_\alpha(\mathbf{r}) = \langle \uparrow | J_\alpha | \uparrow \rangle - \langle \downarrow | J_\alpha | \downarrow \rangle$. Here we took into account that $\langle I_\alpha I_\beta \rangle = \delta_{\alpha\beta} I(I+1)/3$. Sum-

mation by j can be changed to the integration using the standard expression

$$\int F(\mathbf{R}) d\mathbf{R} = v_0 \sum_j F(\mathbf{R}_j). \quad (\text{F4})$$

Using this formula and taking into account that nuclei in GaAs have the same spin, $I_a = I = 3/2$, we finally obtain

$$\langle \Omega_{N,x}^2 \rangle = \frac{v_0 I (I+1) (C_{\text{As}}^2 + C_{\text{Ga}}^2)}{27 \hbar^2} \times \int d\mathbf{r} [j_x^2(\mathbf{r}) + j_y^2(\mathbf{r}) + j_z^2(\mathbf{r})]. \quad (\text{F5})$$

The compact analytical expression for the $\langle \Omega_{N,x}^2 \rangle$ can be derived assuming that $|f(r)|$ exceeds by far $|g(r)|$ in Eqs. (1). Keeping the terms with the lowest powers of $g(r)$, we arrive at

$$\langle \Omega_{N,x}^2 \rangle = \frac{v_0 I (I+1) (C_{\text{As}}^2 + C_{\text{Ga}}^2)}{9\pi \hbar^2} \times \int d\mathbf{r} r^2 \left[\frac{2f(r)^2 g(r)^2}{5} + \frac{3\Delta_1^2 f(r)^4}{4\Delta_0^2} \right]. \quad (\text{F6})$$

It is noteworthy that Eq. (F6) contains two contributions. The second one $\propto (\Delta_1/\Delta_0)^2$ is related to the heavy-hole–light-hole mixing due to the strain and is similar to the one widely studied in quantum dot structures [4,38]. The first contribution results from the complex structure of the acceptor function. This contribution does not require any strain.

Assuming the Gaussian distribution of the nuclear field fluctuations [39], the component of the hole pseudospin normal to magnetic field \mathbf{S}_\perp decays as $\mathbf{S}_\perp \sim \exp(-\langle \Omega_{N,x}^2 \rangle t^2/2)$, the corresponding decay time $T_2^* = \sqrt{2} \langle \Omega_{N,x}^2 \rangle^{-1/2}$. Using Eq. (F6), $C_{\text{As}} = 4.4 \mu\text{eV}$, $C_{\text{Ga}} = 3 \mu\text{eV}$ [38], $\Delta_1/\Delta_0 = 0.05$, $\int d\mathbf{r} r^2 f^2 g^2 = 0.5/a_B^3$, $\int d\mathbf{r} r^2 f^4 = 7.9/a_B^3$, where a_B is the acceptor Bohr radius [24], we obtain $T_2^* \approx 58$ ns for the first contribution in Eq. (F6) and $T_2^* \approx 216$ ns for the second contribution in Eq. (F6). This intrinsic dephasing time originates from the hyperfine interaction with $\sim 5 \times 10^3$ nuclei covered by the hole wave function.

[1] C. Kloeffel and D. Loss, Prospects for spin-based quantum computing in quantum dots, *Annu. Rev. Condens. Matter Phys.* **4**, 51 (2013).
 [2] A. Morello, J. J. Pla, P. Bertet, and D. N. Jamieson, Donor spins in silicon for quantum technologies, *Adv. Quantum Technol.* **3**, 2000005 (2020).
 [3] X. Linpeng, M. L. K. Viitaniemi, A. Vishnuradhan, Y. Kozuka, C. Johnson, M. Kawasaki, and K.-M. C. Fu, Coherence Properties of Shallow Donor Qubits in ZnO, *Phys. Rev. Appl.* **10**, 064061 (2018).
 [4] M. M. Glazov, *Electron & Nuclear Spin Dynamics in Semiconductor Nanostructures*, Series on Semiconductor Science and Technology (Oxford University Press, Oxford, 2018).

[5] D. Brunner, B. D. Gerardot, P. A. Dalgarno, G. Wüst, K. Karrai, N. G. Stoltz, P. M. Petroff, and R. J. Warburton, A coherent single-hole spin in a semiconductor, *Science* **325**, 70 (2009).
 [6] J. H. Prechtel, A. V. Kuhlmann, J. Houel, A. Ludwig, S. R. Valentin, A. D. Wieck, and R. J. Warburton, Decoupling a hole spin qubit from the nuclear spins, *Nat. Mater.* **15**, 981 (2016).
 [7] X. Xu, B. Sun, P. R. Berman, D. G. Steel, A. S. Bracker, D. Gammon, and L. J. Sham, Coherent population trapping of an electron spin in a single negatively charged quantum dot, *Nat. Phys.* **4**, 692 (2008).
 [8] K.-M. C. Fu, C. Santori, C. Stanley, M. C. Holland, and Y. Yamamoto, Coherent Population Trapping of Electron Spins in

- a High-Purity *n*-Type GaAs Semiconductor, *Phys. Rev. Lett.* **95**, 187405 (2005).
- [9] K. D. Greve, P. L. McMahon, D. Press, T. D. Ladd, D. Bisping, C. Schneider, M. Kamp, L. Worschech, S. Höfling, A. Forchel, and Y. Yamamoto, Ultrafast coherent control and suppressed nuclear feedback of a single quantum dot hole qubit, *Nat. Phys.* **7**, 872 (2011).
- [10] A. Delteil, Z. Sun, W. bo Gao, E. Togan, S. Faelt, and A. Imamoglu, Generation of heralded entanglement between distant hole spins, *Nat. Phys.* **12**, 218 (2015).
- [11] H. Watzinger, J. Kukučka, L. Vukušić, F. Gao, T. Wang, F. Schäffler, J.-J. Zhang, and G. Katsaros, A germanium hole spin qubit, *Nat. Commun.* **9**, 3902 (2018).
- [12] R. Muraud, X. Jehl, D. Kotekar-Patil, A. Corna, H. Bohuslavskiy, R. Laviéville, L. Hutin, S. Barraud, M. Vinet, M. Sanquer, and S. D. Franceschi, A CMOS silicon spin qubit, *Nat. Commun.* **7**, 13575 (2016).
- [13] T. Karin, R. J. Barbour, C. Santori, Y. Yamamoto, Y. Hirayama, and K.-M. C. Fu, Radiative properties of multicarrier bound excitons in GaAs, *Phys. Rev. B* **91**, 165204 (2015).
- [14] D. J. Hilton and C. L. Tang, Optical Orientation and Femtosecond Relaxation of Spin-Polarized Holes in GaAs, *Phys. Rev. Lett.* **89**, 146601 (2002).
- [15] L. Viña, T. C. Damen, J. E. Cunningham, J. Shah, and L. J. Sham, Spin relaxation dynamics in GaAs quantum wells: Free carriers and excitons, *Superlattices Microstruct.* **12**, 379 (1992).
- [16] D. Heiss, S. Schaeck, H. Huebl, M. Bichler, G. Abstreiter, J. J. Finley, D. V. Bulaev, and D. Loss, Observation of extremely slow hole spin relaxation in self-assembled quantum dots, *Phys. Rev. B* **76**, 241306(R) (2007).
- [17] S. L. Chuang, *Physics of Photonic Devices* (Wiley, Hoboken, NJ, 2009).
- [18] In these estimates, we disregarded the renormalization of the deformation potential due to the Coulomb potential of the acceptor [31]; this effect is discussed in more detail below in relation to the spin-flip of the hole.
- [19] E. J. Stanton, J. Chiles, N. Nader, G. Moody, N. Volet, L. Chang, J. E. Bowers, S. W. Nam, and R. P. Mirin, Efficient second harmonic generation in nanophotonic GaAs-on-insulator waveguides, *Opt. Express* **28**, 9521 (2020).
- [20] X. Yuan, F. Weyhausen-Brinkmann, J. Martin-Sanchez, G. Piredda, V. Krápek, Y. Huo, H. Huang, C. Schimpf, O. G. Schmidt, J. Edlinger, G. Bester, R. Trotta, and A. Rastelli, Uniaxial stress flips the natural quantization axis of a quantum dot for integrated quantum photonics, *Nat. Commun.* **9**, 3058 (2018).
- [21] X. Linpeng, T. Karin, M. V. Durnev, R. Barbour, M. M. Glazov, E. Ya. Sherman, S. P. Watkins, S. Seto, and K.-M. C. Fu, Longitudinal spin relaxation of donor-bound electrons in direct band-gap semiconductors, *Phys. Rev. B* **94**, 125401 (2016).
- [22] S. E. Harris, Electromagnetically induced transparency, *Phys. Today* **50**, 36 (1997).
- [23] B. D. Agap'ev, M. B. Gornyi, B. G. Matisov, and Yu. V. Rozhdestvenskii, Coherent population trapping in quantum systems, *Phys. Usp.* **36**, 763 (1993).
- [24] A. Baldereschi and N. O. Lipari, Spherical model of shallow acceptor states in semiconductors, *Phys. Rev. B* **8**, 2697 (1973).
- [25] B. L. Gelmont and M. I. Dyakonov, Acceptor levels in diamond-type semiconductors, *Sov. Phys. Semicond.* **5**, 1905 (1972).
- [26] B. L. Gelmont and M. I. Dyakonov, *g*-factor of acceptors in zinc-blende semiconductors, *Sov. Phys. Semicond.* **7**, 1345 (1973).
- [27] A. V. Malyshev and I. A. Merkulov, Magnetic moment of an acceptor center in cubic semiconductors, *Phys. Solid State* **39**, 49 (1997).
- [28] X. Marie, T. Amand, P. Le Jeune, M. Paillard, P. Renucci, L. E. Golub, V. D. Dymnikov, and E. L. Ivchenko, Hole spin quantum beats in quantum-well structures, *Phys. Rev. B* **60**, 5811 (1999).
- [29] L. M. Woods, T. L. Reinecke, and R. Kotlyar, Hole spin relaxation in quantum dots, *Phys. Rev. B* **69**, 125330 (2004).
- [30] G. L. Bir and G. E. Pikus, *Symmetry and Strain-induced Effects in Semiconductors* (Wiley, New York, 1974).
- [31] Sh. M. Kogan and A. F. Polupanov, Optical absorption and photoeffect spectra of shallow acceptor impurities in semiconductors, *Zh. Eksp. Teor. Fiz.* **80**, 394 (1981) [*JETP* **53**, 201 (1981)].
- [32] D. Bimberg, Anomaly of the linear and quadratic Zeeman effect of an effective-mass acceptor: C in GaAs, *Phys. Rev. B* **18**, 1794 (1978).
- [33] V. E. Kirpichev, I. V. Kukushkin, V. E. Bisti, K. von Klitzing, and K. Eberl, Magneto-optic measurements of the cyclotron mass and *g*-factor of light holes in GaAs, *JETP Lett.* **64**, 814 (1996).
- [34] H. M. G. A. Tholen, J. S. Wildmann, A. Rastelli, R. Trotta, C. E. Pryor, E. Zallo, O. G. Schmidt, P. M. Koenraad, and A. Yu. Silov, Active tuning of the *g*-tensor in In-GaAs/GaAs quantum dots via strain, *Phys. Rev. B* **99**, 195305 (2019).
- [35] M. Bayer, G. Ortner, O. Stern, A. Kuther, A. A. Gorbunov, A. Forchel, P. Hawrylak, S. Fafard, K. Hinzer, T. L. Reinecke, S. N. Walck, J. P. Reithmaier, F. Kloppe, and F. Schäfer, Fine structure of neutral and charged excitons in self-assembled In(Ga)As/(Al)GaAs quantum dots, *Phys. Rev. B* **65**, 195315 (2002).
- [36] E. A. Chekhovich, M. M. Glazov, A. B. Krysa, M. Hopkinson, P. Senellart, A. Lemaître, M. S. Skolnick, and A. I. Tartakovskii, Element-sensitive measurement of the hole-nuclear spin interaction in quantum dots, *Nat. Phys.* **9**, 74 (2013).
- [37] M. Vidal, M. V. Durnev, L. Bouet, T. Amand, M. M. Glazov, E. L. Ivchenko, P. Zhou, G. Wang, T. Mano, T. Kuroda, X. Marie, K. Sakoda, and B. Urbaszek, Hyperfine coupling of hole and nuclear spins in symmetric (111)-grown GaAs quantum dots, *Phys. Rev. B* **94**, 121302(R) (2016).
- [38] C. Testelin, F. Bernardot, B. Eble, and M. Chamarro, Hole-spin dephasing time associated with hyperfine interaction in quantum dots, *Phys. Rev. B* **79**, 195440 (2009).
- [39] I. A. Merkulov, A. L. Efros, and M. Rosen, Electron spin relaxation by nuclei in semiconductor quantum dots, *Phys. Rev. B* **65**, 205309 (2002).